

Measuring redshifts using X-ray spectroscopy of galaxy clusters: results from Chandra data and future prospects

H. Yu^{1,2}, P. Tozzi^{2,3}, S. Borgani^{4,3}, P. Rosati⁵, Z.-H. Zhu¹

¹ Department of Astronomy, Beijing Normal University, Beijing 100875, China

² INAF Osservatorio Astronomico di Trieste, via G.B. Tiepolo 11, I-34143, Trieste, Italy

³ INFN– National Institute for Nuclear Physics, Trieste, Italy

⁴ Dipartimento di Fisica dell’Università di Trieste, via G.B. Tiepolo 11, I-34131, Trieste, Italy

⁵ ESO - European Southern Observatory, Karl-Schwarzschild Str. 2, D-85748 Garching b. Munchen, Germany

Preprint online version: January 12, 2013

ABSTRACT

Context. The ubiquitous presence of the Fe line complex in the X-ray spectra of galaxy clusters offers the possibility of measuring their redshift without resorting to spectroscopic follow-up observations. In practice, the blind search of the Fe line in X-ray spectra is a difficult task and is affected not only by limited S/N (particularly at high redshift), but also by several systematic errors, associated with varying Fe abundance values, ICM temperature gradients, and instrumental characteristics.

Aims. We assess the accuracy with which the redshift of galaxy clusters can be recovered from an X-ray spectral analysis of Chandra archival data. We present a strategy to compile large surveys of clusters whose identification and redshift measurement are both based on X-ray data alone.

Methods. We apply a blind search for K-shell and L-shell Fe line complexes in X-ray cluster spectra using Chandra archival observations of galaxy clusters. The Fe line can be detected in the ICM spectra by simply analyzing the C-statistics variation ΔC_{stat} as a function of the redshift parameter, when all the other model parameters are frozen to the best-fit values. We repeat the measurement under different conditions, and compare the X-ray derived redshift z_X with the one obtained by means of optical spectroscopy z_o . We explore how a number of priors on metallicity and luminosity can be effectively used to reduce catastrophic errors. The ΔC_{stat} provides the most effective means for discarding wrong redshift measurements and estimating the actual error in z_X .

Results. We identify a simple and efficient procedure for optimally measuring the redshifts from the X-ray spectral analysis of clusters of galaxies. When this procedure is applied to mock catalogs extracted from high sensitivity, wide-area cluster surveys, such as those proposed with Wide Field X-ray Telescope (WFXT) mission, it is possible to obtain complete samples of X-ray clusters with reliable redshift measurements, thus avoiding time-consuming optical spectroscopic observations. Our analysis shows that, in the case of WFXT, a blind Fe line search is 95% successful for spectra with more than 1000 net counts, whenever $\Delta C_{stat} > 9$, corresponding formally to a 3σ confidence level. The average error in the redshift z_X decreases rapidly for higher values of ΔC_{stat} . Finally, we discuss how to estimate the completeness of a large cluster samples with measured z_X . This methodology will make it possible to trace cosmic growth by studying the evolution of the cluster mass function directly using X-ray data.

Key words. galaxies: clusters: general – cosmology: observations – X-ray: galaxies: clusters – intracluster medium

1. Introduction

The study of clusters of galaxies allows one to investigate the large-scale structure of the Universe, constrain the cosmological parameters and the spectrum of the primordial density fluctuations, and study the interactions between the member galaxies and the ambient intra cluster medium (ICM, see Rosati et al. 2002; Schuecker 2005; Voit 2005; Borgani 2006; Tozzi 2007; Vikhlinin et al. 2009; Mantz et al. 2010; Böhringer & Werner 2010). The X-ray band is an optimal observational window for identifying and studying clusters of galaxies. The thermal bremsstrahlung emission due to the hot diffuse ICM is roughly proportional to the baryon density squared. This makes clusters of galaxies prominent sources in the X-ray sky.

Thanks to the spatial resolution of Chandra and the high sensitivity of XMM, coupled with their excellent spectral resolutions, it has become possible to study the detailed thermodynamical properties of the ICM. In particular, the detection of emission lines of highly ionized metals, in both the core and outer

regions of groups and clusters, has proven to be very efficiency in investigating the chemical properties of the ICM. Indeed, the ubiquitous presence of the K-shell Fe line complex at 6.7-6.9 keV, which was first detected by Mitchell et al. (1976), has been detected at the highest redshift $z \sim 1.4$ where X-ray clusters have been observed (see Rosati et al. 2004; Stanford et al. 2005; Rosati et al. 2009). In principle, abundance measurements based on the detection of the Fe line also provide a way to measure the position of the Fe line, thus the cluster redshift.

A few redshifts have been measured using X-ray spectral analyses in cases of no previous optical spectroscopic observations (Hashimoto et al. 2004; Lamer et al. 2008). But, this approach has never been used systematically in cluster surveys.¹ The main reason is that most of the existing cluster surveys

¹ We note that a blind survey of the 6.4 Fe line has been applied to AGN X-ray surveys with interesting results (Maccacaro et al. 2004; Braito et al. 2005). The search of line emission in deep AGN surveys, however, is significantly different with respect to the search of Fe line emission in the thermal spectra of ICM, and their method is unsuitable in our case.

are based on source samples selected by ROSAT, whose energy range is 0.1–2.4 keV, hence does not cover the hard band where the Fe lines lie. To date, most ROSAT clusters have been confirmed through optical imaging and spectroscopic observations. Several studies based on Chandra and XMM data (Tozzi et al. 2003; Ettori et al. 2004; Balestra et al. 2007; Maughan et al. 2008) simply confirmed the excellent agreement of X-ray and optical redshifts. This agreement was achieved using the optical redshift as the initial redshift parameter in the X-ray spectral fit. The blind search of the redshift from the X-ray spectral analysis has never been explored thoroughly.

The situation could change significantly with the next-generation X-ray surveys of planned future missions sensitive in the 0.5–10 keV band, such as eROSITA (Predehl et al. 2010) or the proposed Wide Field X-ray Telescope (WFXT, see Murray & WFXT Team 2010). In these surveys, we expect to detect several hundred thousands of groups and clusters of galaxies, making an *ad hoc* follow-up program infeasible, and requiring careful coordination with existing and future optical and IR surveys (Rosati et al. 2010). Therefore, the ability to recover redshifts on the basis of the X-ray data alone, would be critical since it would allow one to measure the redshift, thus the intrinsic physical properties of ICM, such as the X-ray luminosity L_X , ICM temperature T_X , iron abundance of the ICM Z , and the electron density n_e . In this case, it will be not only possible to investigate the physics of the ICM, but also perform cosmological tests with large cluster surveys entirely characterized on the basis of X-ray data.

The factors which affect the measurement of redshift from X-ray spectra are: the signal-to-noise ratio, hereafter S/N (or the total number of detected counts), the energy dependence of the instrument effective area, its spectral resolution, the intrinsic Fe abundance (or metallicity in general), the ICM temperature, and the actual redshift. A possible departure from collisional equilibrium, or the incompleteness of the atomic models used in the fitting procedure, are not investigated here, and are expected to be negligible in the analysis of high- z cluster spectra. In this work, we use the data archive of the Chandra X-ray satellite to investigate the ability of recovering the X-ray redshift z_X with a blind search of X-ray emission lines. This can lead to interesting applications for future X-ray survey missions.

The paper is organized as follows: in Section 2, we describe the data we use for our study. In Section 3, we present a simple and efficient strategy to search for emission lines in X-ray spectra. In Section 4, we explore the use of weak priors to test their effect on X-ray redshift measurements. In Section 5, we apply our algorithm to the expected results from the WFXT surveys. Finally in Section 6, we summarize our conclusions. Throughout the paper, we assume the 7-year WMAP cosmology $\Omega_\Lambda = 0.728$, $\Omega_m = 0.272$, and $H_0 = 70.4 \text{ km s}^{-1} \text{ Mpc}^{-1}$ (Komatsu et al. 2010).

2. The data

We searched the Chandra archive for targeted observations of galaxy clusters with different temperatures and redshifts. We adopted a sample of 46 clusters (see Table 1) mostly based on those studied by Balestra et al. (2007). This sample includes clusters with temperatures from $\sim 4 \text{ keV}$ to $\sim 14 \text{ keV}$ over a wide redshift range ($0.16 < z < 1.4$). The sample is incomplete and represents a collection of targets from different surveys (see reference list in Table 1). We also remark that in several cases we did not make use of all the available archival observations, in order to explore a wider S/N range. However, the most impor-

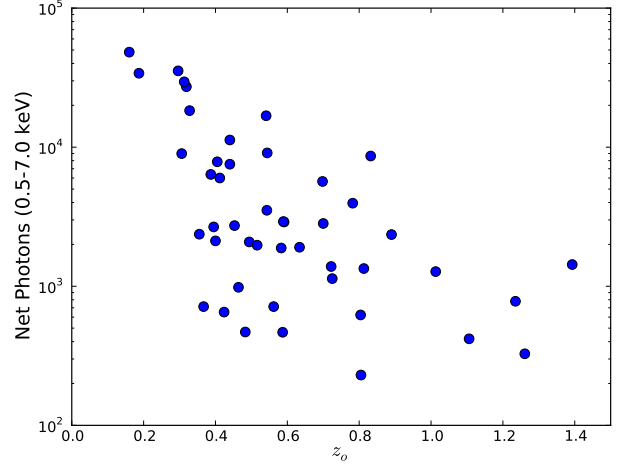


Fig. 1: Detected photons as a function of redshift for the 46 clusters selected from the Chandra archive. The wide range of values reflects the different fluxes of each object and the different exposure times of the available data.

tant point is that this sample covers a sizable portion of redshift-temperature space allowing us to comprehensively explore the ability to measure the redshifts from the X-ray spectra.

The number of detected photons in the 0.5–7 keV band ranges from ~ 230 to ~ 45000 as shown in Figure 1. Most were gathered with Chandra ACIS-I in the FAINT/VERYFAINT mode, while only six clusters were observed with ACIS-S. Calibration files were obtained using the most recent release of CALDB at the time of writing (CALDB 4.2). Image reduction began from the level 1 event file. We applied a charge transfer inefficiency (CTI) correction, FAINT/VERYFAINT cleaning, grade correction, and time-dependent gain correction. High background intervals were filtered with a 3σ clipping procedure. The response matrix files (RMF) and the ancillary response files (ARF), necessary for the X-ray spectral analysis, were generated with `mkacisrmf` and `mkwarf`. For details about data reduction, we refer to Balestra et al. (2007).

The spectra were analyzed with XSPEC v12.6.0 (Arnaud 1996). Data were fitted with a single-temperature `mekal` model (Mewe et al. 1985, 1986; Kaastra 1992; Liedahl et al. 1995) in which the ratio of the elements was fixed to the solar value as in Anders & Grevesse (1989). Galactic absorption is modeled with `tbabs` (Wilms et al. 2000). The optical redshifts were collected from the literature. The typical error in the optical redshift is $\Delta z \sim 0.003$. We adopt the optical redshift when measuring the temperatures and metallicities of the ICM. Our results, shown in Table 1, differ slightly from previous analyses presented in Balestra et al. (2007) because of the updated Chandra calibration and in some cases the different extraction region. Computed errors always correspond to the 1σ confidence level.

3. Blind search for the redshift with no priors

3.1. Method

The K_α shell complex of Fe consists of two groups of lines. The first is the He-like iron (Fe XXV) K-shell complex, whose resonant line is at 6.7 keV, that is the most prominent spectral feature of ICM spectra at high temperatures (above 2 keV). The second group corresponds to the H-like iron (Fe XXVI) spectral

line whose resonant line is at 6.9 keV. Both groups include lines corresponding to several transitions as predicted in the case of collisional ionization equilibrium. The H-like and He-like complexes, separated by about 0.2 keV, can be resolved at the spectral resolution of Chandra ACIS in data of high S/N; in this case, the line ratio can be used as a temperature diagnostic in addition to the continuum shape. On the other hand, the structure of each group is not resolved and reflects the asymmetric shape of the observed feature. Both effects are taken into account by the *mekal* model, which includes excitation, radiative recombination, dielectronic recombination, and inner shell ionization, and assumes the optically thin limit (i.e., that no photo-ionization or photo-excitation effects are taken into account). Given the low S/N of distant cluster spectra, the K_α line complex often appears as a single, prominent feature.

Owing to uncertainties in the ACIS calibration below 0.5 keV, we excluded these low energy photons from the spectral analysis to avoid any systematic bias. The effective cut at high energies is generally around 7 keV, since the S/N of a thermal spectrum rapidly decreases above 5 keV. Therefore, we consider the energy range 0.5-7 keV for both imaging and spectral analysis. Given the explored redshift interval ($0 < z < 2$), the Fe line complex is always well within this range.

Background is usually selected in the same chip where the source lies. When several observations are used, the background can only be selected in overlapping regions. For some nearby clusters that occupy a whole chip, or even an entire field (Abell 1689 for example), we compile a synthetic background using CALDB. The centroid of the cluster emission is determined by surface brightness fits adopting a standard β model (Cavaliere & Fusco-Femiano 1976). A set of circular regions are then drawn to select the extraction radius R_{ext} that maximizes the S/N, computed as $SN(R) = (S(R) - B) / \sqrt{S(R) + (A_S/A_B) \times B}$, where $S(R)$ are the total number of photons detected within the radius R , and B are the background number of photons expected in the same area. The factor A_S/A_B is the geometrical backscale, i.e. the ratio of the area of the source extraction region to that of the background. Since our sources are extended and the background is chosen to be as close as possible to the source, this factor can be of order ≤ 1 . This expression properly takes into account the statistical uncertainty in the number of photons in the source region and the region where the background is sampled. The extraction regions are selected on the X-ray image in the total band (0.5-7 keV).

We adopt the default Levenberg-Marquardt fitting algorithm. There are four parameters to be fitted: temperature, metal abundance, redshift, and normalization. To test the capability of recovering the actual redshift with a blind search of the K_α Fe line in the X-ray spectrum, we repeat our fits starting from a reference set of parameters, corresponding to $z_{start} = 0.1$, $kT_{start} = 5$ keV, and $Z_{start}/Z_\odot = 0.3$ in units of Anders & Grevesse (1989) for all the clusters. We use Cash statistics (Cash 1979) applied to an unbinned source plus background counts, and therefore exploit the full spectral resolution of the ACIS-I and ACIS-S instrument. Cash statistics ensure better performance with respect to the canonical χ^2 analysis of binned data, particularly for low S/N spectra (Nousek & Shue 1989). After finding the absolute minimum, we explore the redshift space with the *steppar* command, covering the entire range of possible values from $z = 0.01$ to $z = 2.0$ with a very small step $\delta z = 0.01$. When a new minimum is obtained, the best fit is automatically updated. We then plot the difference of the C-stat value with respect to the minimum as a function of redshift. The $\Delta C_{stat}(z)$ function is therefore the difference between the absolute minimum and the

best-fit value obtained when the z parameter does not match any line, which is equivalent to optimizing the fit when the Fe abundance is forced to be zero. One example (MACSJ1423) is shown in Figure 2. The ΔC_{stat} rapidly declines to a minimum whenever a Fe line candidate is found. The deepest minimum in the C-statistics as a function of the redshift in Figure 2 clearly shows that the best-fit redshift agrees with the optical redshift (indicated by the vertical line). The horizontal line, therefore, corresponds to the minimum C_{stat} value obtained with zero metal abundance.

The case of a catastrophic error is shown in Figure 3. Here there are no minima corresponding to the optical redshift. We note that, instead, there are several comparable secondary minima. We explore a possible use of secondary minima in Section 3.7.

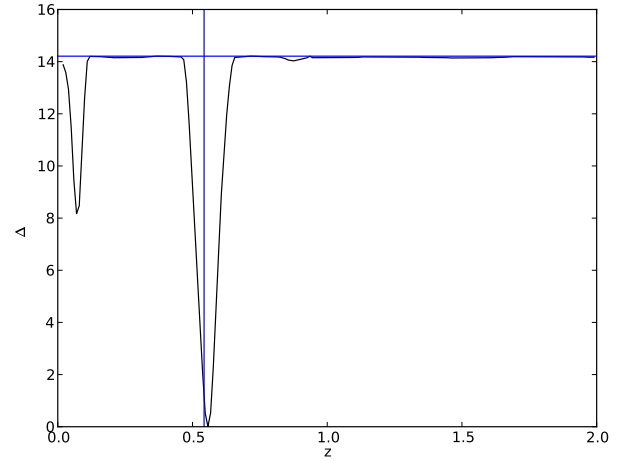


Fig. 2: ΔC_{stat} as a function of the redshift parameter for MACSJ1423. The vertical line indicates the optical redshift. The horizontal line corresponds to the minimum C_{stat} allowed when the metal abundance is set to zero.

3.2. Results

For most clusters, the redshifts z_X found from the X-ray spectral analysis are consistent with their optical values z_o within the errors as shown in Figure 4. However, there are still several clusters for which z_X is far from z_o . To define these “catastrophic failures”, we perform a 3σ -clipping by computing the rms value $\Delta z_{rms} \equiv \sqrt{\sum (z_X - z_o)^2 / n}$ for the entire sample of 46 clusters. The catastrophic errors are shown as empty circles in Figure 4 and as an empty histogram in Figure 5, where we plot the quantity $\Delta z / \Delta z_{rms}$. Thanks to this definition, we identify eight catastrophic errors. After removing the catastrophic failures, the rms redshift deviation is $\Delta z \sim 0.03$. We note that this uncertainty is somewhat larger than the typical statistical error σ_z estimated by the XSPEC fitting routine. We argue that the statistical error in the redshift is slightly underestimated. As we see later (Section 5.1), ΔC_{stat} is not only the most relevant parameter to accept or reject the z_X value, but can also be used to adjust the statistical error obtained by the spectral fit thanks to its strong correlation with the actual value of $z_X - z_o$.

Our results for the entire sample of *Chandra* clusters is shown in Table 2. From a comparison with Table 1, it is pos-

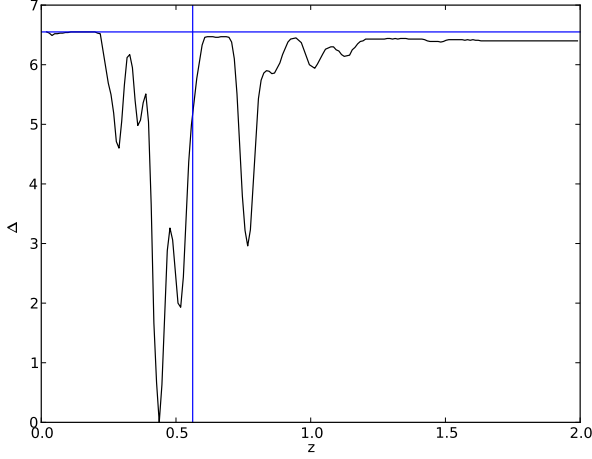


Fig. 3: ΔC_{stat} as a function of the redshift parameter for SC1120. The vertical line indicates the optical redshift. At variance with Figure 2, the search for a minimum in C_{stat} leads to a catastrophic error.

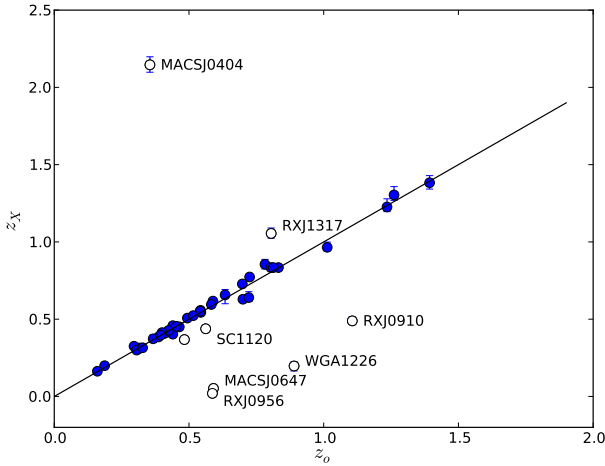


Fig. 4: X-ray redshift z_X compared to the optical values z_o for the 46 Chandra clusters in our sample. The eight empty circles are the catastrophic failures selected with a 3σ clipping.

sible to see that, apart from the catastrophic failures, the best-fit temperatures are unaffected, while the best-fit metal abundances are systematically higher (see discussion in Section 3.5).

3.3. Tuning the energy band

The K_α Fe line is always located in the 2-7 keV energy range (observing frame). Therefore, before analyzing in detail our results, we investigate whether focusing on this band may only help in driving the best-fit redshift value more efficiently towards the real one. We can either select the extraction region from the hard band image, or fit the spectrum in the hard energy band only, or adopt both criteria. The hard-band selected regions are usually smaller since the bulk of the X-ray photons from the ICM thermal spectrum are in the soft (0.5-2 keV) band. To compare the results of different strategies, we introduce a quality param-

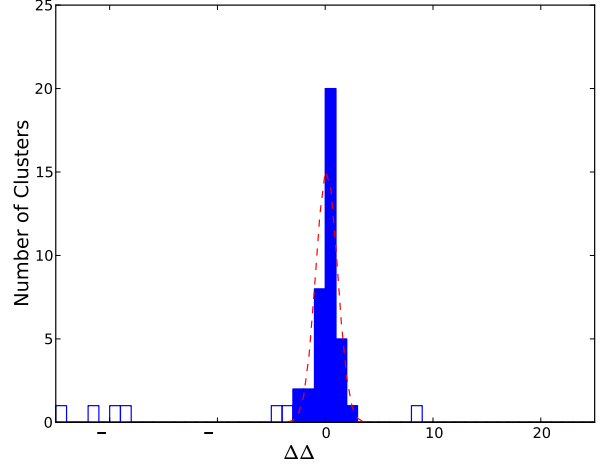


Fig. 5: Histogram of the quantity $\Delta z / \Delta z_{rms}$. Catastrophic failures, identified with a 3σ clipping, are shown with an empty histogram. A Gaussian fit to the data is shown as a dashed line.

Region	Energy band	Q	Δz_{rms}	# of cat. errors
Total	Total	133.60	0.0288	8
Total	Hard	252.79	0.0378	7
Hard	Total	284.14	0.1736	6
Hard	Hard	468.66	0.0356	11

Table 3: Quality parameter for different choices of the energy band and typical rms value of Δz after applying the 3σ clipping.

eter defined as $Q \equiv \sum [(z_{X,i} - z_{o,i}) / \sigma_{z_X}]^2 / n$, where the sum is performed for the entire sample (46 clusters) without removing the catastrophic failures. The value of Q is a useful estimate of the average discrepancy between z_X and z_o obtained with different algorithms. The comparison is shown in Table 3, where we also list the Δz_{rms} values after applying 3σ clipping, and the number of catastrophic failures. We find that our default choice based on the total energy band (0.5-7 keV) has a clear advantage with respect to strategies focusing on the hard band. We argue that the signal in the soft band is useful for defining at best the continuum, and this, in turn, positively affects the detection of the Fe line. We therefore conclude that there is no gain in restricting the energy band to the 2-7 keV range, and that the full amount of spectral information is useful in searching for the Fe K_α line.

3.4. Dependence on the net detected photons

We investigate how the average deviation and the number of catastrophic failures depend on the S/N of the spectra or, alternatively, on the total number of net detected photons. In Figure 6, we show the quantity $z_X - z_o$ as a function of the net detected photons. From the inspection of Figure 6, we note that it is unclear whether a threshold on the number of detected photons exists above which the X-ray redshift can be considered reliable within a given confidence level. When we consider S/N instead, a similar result is obtained. We note that above a threshold of about 1000 counts (vertical line) the number of catastrophic failures is not negligible, although five out of eight catastrophic failures are below this threshold. Three catastrophic errors occur in spectra with thousands of counts. We draw the conclusion that

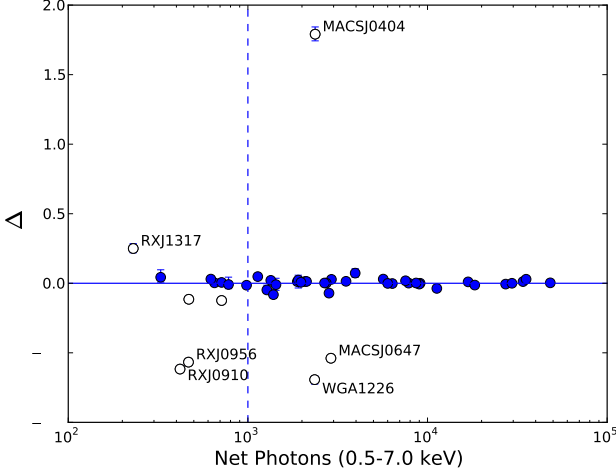


Fig. 6: Difference between optical and X-ray redshifts as a function of the detected photons. The eight empty circles are catastrophic failures. In some cases, spectra of high S/N (e.g. with more than 1000 net photons, shown with a vertical line) may not be successfully fitted.

the efficiency of measuring the redshift depends not only on the high quality of the signal, but also on the intrinsic properties of the source. The likelihood of obtaining a reliable spectral characterization, including the redshift, does not depend only on the net number of photons. To find a robust method to select reliable X-ray redshifts, we proceed with a deeper investigation of the spectral parameters. The most obvious parameter to consider is the actual Fe abundance.

3.5. Dependence on the intrinsic metal abundance

We explore now whether the intrinsically low Fe abundance can be another relevant source of error. In Figure 7, we plot the “true” Fe abundance Z_{Fe} (i.e., the value obtained when the redshift is fixed to the optical value, see Table 1) versus the number of net detected photons in each spectrum. Most catastrophic failures are located in the bottom-left corner. This indicates that the largest discrepancies are associated with both the low S/N of the X-ray spectrum and the low Fe abundance. Significant discrepancies can be found among spectra with more than ~ 4000 photons if the Fe abundance is $Z_{Fe} \leq 0.2Z_{\odot}$.

This information cannot be used in our blind search for the emission lines, since we do not know a priori, the Fe abundance. As we see in the next section, making an assumption about the intrinsic Z_{Fe} value does not improve the fit. In any case, we find that it is impossible to use a sample whose redshift is determined via the X-ray analysis to investigate the Fe abundance. The X-ray fits with a free redshift parameter will always lead to values that are systematically higher than those obtained by fixing the redshift to the optical value z_o , as shown in Figure 8. We find that the typical value of the ratio of the fitted Fe abundance to the “true” one is $\langle Z_{Fe}(z_X)/Z_{Fe}(z_o) \rangle = 1.110$, which corresponds to a positive bias of 11%. This result is expected since the position of the Fe line is found by maximizing the Fe abundance for a given temperature. On the other hand, there is no evidence of a bias in the best-fit values of the temperature, as shown in Figure 9. For the temperature ratio, we find that $\langle T(z_X)/T(z_o) \rangle = 0.993$.

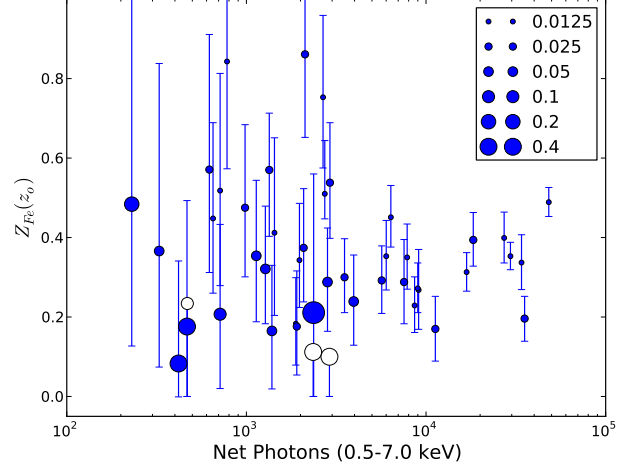


Fig. 7: “True” Fe abundance (obtained by fitting the X-ray spectra freezing the redshift to the optical value) versus the total number of detected photons. The radius of the dots is proportional to $|\Delta z|$. The three empty circles represent 1σ upper limits.

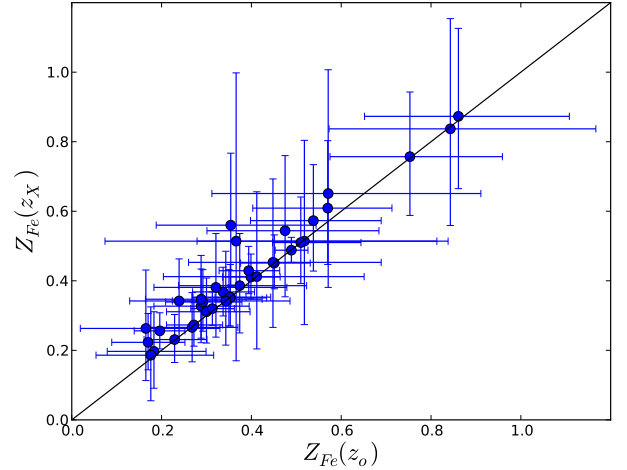


Fig. 8: “True” Fe abundances $Z_{Fe}(z_o)$ in the Chandra sample (obtained by fixing the redshift parameter to the optical value) plotted against those measured leaving the redshift parameter free. Catastrophic failures are not included. The values of $Z_{Fe}(z_X)$ are systematically higher than those we derive when the redshift is fixed to the optical value.

3.6. Dependence on ΔC_{stat}

Another important indication is the intensity of the emission line itself. The most reliable lines are those that provide the largest decrease ΔC_{stat} in the C-statistics (see Figure 2). A larger ΔC_{stat} indicates a more robust emission line, then a more reliable X-ray redshift, as shown in Figure 10. Assuming that ΔC_{stat} behaves similarly to the $\Delta\chi^2$ for one degree of freedom, we find that a threshold that excludes all the catastrophic errors is $\Delta C_{stat} > 9$, corresponding to a nominal confidence level of 3σ . Above this level, we have 26 clusters for which the redshift is measured with good accuracy, constituting a sample virtually free of catastrophic errors.

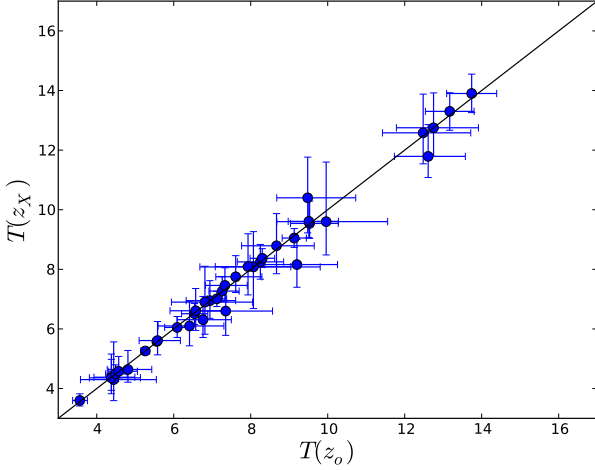


Fig. 9: "True" temperature $T(z_o)$ (obtained when the redshift parameter is fixed to the optical value z_o) plotted against the value $T(z_X)$ measured leaving the redshift parameter free. Catastrophic failures are not included.

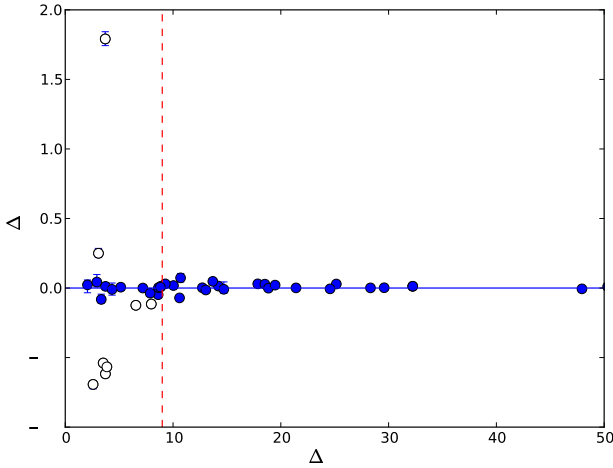


Fig. 10: The quantity $\Delta z = z_X - z_o$ plotted against ΔC_{stat} . The eight empty circles are catastrophic failures. The vertical line shows the nominal 3σ threshold corresponding to $\Delta C_{stat} = 9$.

3.7. Exploring the secondary minima

We have investigated the properties of the absolute minima. In principle, the C_{stat} function of each cluster has several secondary minima that may contain useful information. We explore this possibility by identifying all the local minima in the $C_{stat} - z$ function, and considering the corresponding ΔC_{stat} and Δz . We find that, as for the catastrophic failure, none of their secondary minima provide a correct redshift measurement. As for the 38 clusters with acceptable redshift measurements, secondary minima do not provide any improvement in the redshift value, as expected.

We also explore the possibility of flagging unreliable z_X from the presence of one or more secondary minima close to the absolute minimum. However, applying a naive rejection based on more than one line of similar ΔC_{stat} , would result in the rejection of several successful cases.

In summary, we do not find any benefit when considering the secondary minima, and we confirm that simply using a sharp threshold on ΔC_{stat} is the most efficient criterion for selecting reliable redshift measurements.

4. Refining the strategy with weak priors

We have previously here applied a direct blind search for the Fe line without making any further assumption. We now investigate whether we can achieve a more efficient strategy using weak priors. Two possible choices of priors come from the study of local cluster samples: the low scatter in the measured Fe abundance of hot clusters and the tightness of the $L - T$ relation.

4.1. Prior on the Fe abundance

The Fe abundance is observed to be almost constant in local and medium redshift clusters for virial temperatures $kT > 5$ keV (Renzini 1997; Baumgartner et al. 2005; Balestra et al. 2007). This suggests that we may remove one fitting parameter by freezing the Fe abundance to $Z_{Fe} = 0.3Z_{\odot}$. This assumption would be wrong below 3 keV, since in the low temperature range (from poor clusters to groups) the Fe abundance values cover a wide range (Renzini 1997; Rasmussen & Ponman 2007). To explore the effects of this assumption, we repeat the fits with $Z = 0.3Z_{\odot}$ and show the results in Figure 11. The Q value after this assumption is 103.12, which represents a mild improvement in accuracy, mainly because of the larger error bars of MACSJ0404 and RXJ0542. Incidentally, we note that these two clusters with "true" Fe abundance below $0.2Z_{\odot}$ are fitted with a redshift ~ 2.1 , a mistake caused by an edge in the Chandra response around 2 keV. The average rms value of Δz is also 0.03, and the number of catastrophic failures is 9. We conclude that there is no evidence that a prior on the Fe abundance provide more reliable results. In addition, we find some indication that this assumption might prevent us from being able to use the criterion about ΔC_{stat} to select the most reliable redshift measurements, as shown in Figure 12, where we have two catastrophic failures for $\Delta C_{stat} > 9$.

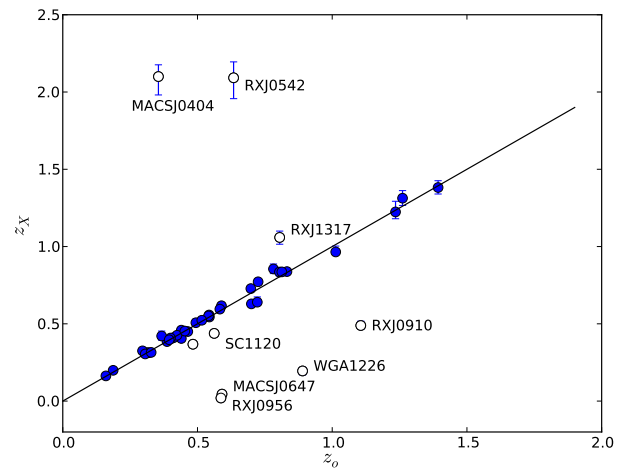


Fig. 11: Same as Figure 4, after assuming a fixed Fe abundance $Z_{Fe} = 0.3Z_{\odot}$.

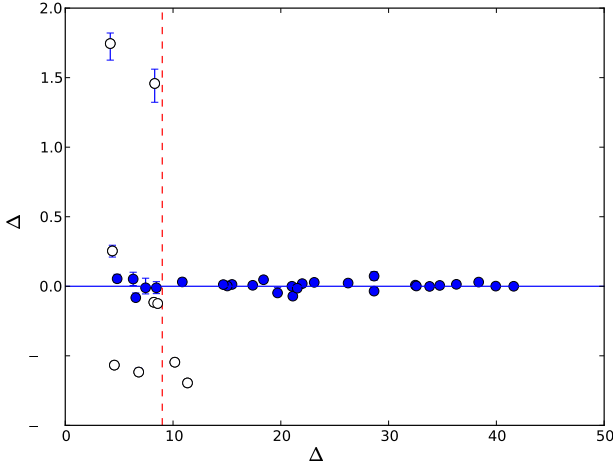


Fig. 12: Same as Figure 10, after assuming a fixed Fe abundance $Z_{Fe} = 0.3Z_{\odot}$.

4.2. Priors on the $L - T$ relation

Additional information is the clearly defined $L - T$ relation measured for local groups and clusters of galaxies (see, e.g., Lumb et al. 2004; Maughan et al. 2006; Pratt et al. 2009). Large errors in the redshift will result in a position in the $L - T$ plane significantly distant from the average observed relation, once the intrinsic scatter is properly taken into account.

To illustrate this effect, we compute the bolometric luminosities for our sample of clusters. The luminosity contribution outside the extraction regions is estimated by fitting a β model to the observed surface brightness. All luminosities are computed for R_{500} , which is defined as the radius within which the average density contrast is 500 times the critical density of the universe at the cluster redshift. As for the $L-T$ relation, we adopt the best fit by Maughan et al. (2006) to the Wide Angle ROSAT Pointed Survey (WARPS) sample at $0.6 < z < 1.0$:

$$L_{500} = 4.97 \pm 0.80 \left(\frac{kT}{6 \text{ keV}} \right)^{2.80 \pm 0.55} 10^{44} h_{70}^{-2} \text{ erg s}^{-1}. \quad (1)$$

In Figure 13, we compare this relation with that obtained with our cluster sample in a similar redshift range. Catastrophic failures are labeled with empty circles. In total 14 clusters, including six catastrophic errors, are formally excluded if we require all the clusters to be consistent at the 3σ level with the assumed $L-T$ relation. We note, indeed, that the catastrophic errors are generally distant from the measured $L-T$ relation, but still very close to the bulk of the cluster, so that a clear separation is not observed. This happens because the fitted temperature scales as $(1 + z_X)$, and the relation is approximately $L \propto T^3$. This implies that a wrong redshift would move the cluster luminosity approximately along the observed $L - T$ relation. Another less relevant constraint that we show in Figure 13 is an upper limit on the ICM temperature, which is conservatively put to 20 keV (corresponding to the $3 - 8 \times 10^{15} M_{\odot}$ range). This constraint is expected to be useful in only a few extreme cases.

In principle, this prior should be applied at different redshifts because the $L - T$ relation and its intrinsic scatter are expected to evolve at some level. However, there is still significant uncertainty in the measured $L-T$ evolution (see Ettori et al. 2004;

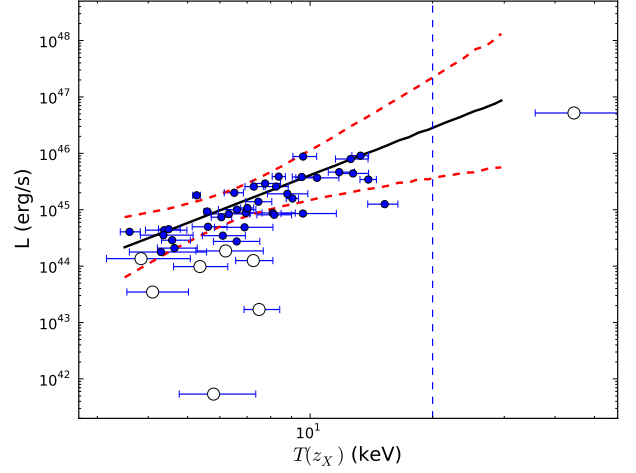


Fig. 13: $L-T$ relation for our cluster sample compared with the relation measured by Maughan et al. (2006). Catastrophic failures are marked as empty circles. The red dashed lines indicate the 3σ confidence levels around the average $L-T$ relation. The vertical dashed line marks a reasonable upper limit (20 keV) that can be assumed for ICM temperatures.

Maughan et al. 2006; Branchesi et al. 2007). To summarize, the $L-T$ prior can be effective given that slope, normalization, and intrinsic scatter are accurately known at different redshifts. In practice, this kind of information is expected to be obtained from cluster samples as large as those achievable with future wide area surveys. In this case, this criterion would not be a prior, but rather a self-calibration procedure. Therefore, with the present knowledge this prior should be applied with caution.

5. Building a complete sample of clusters with measured z_X : application to future X-ray surveys

The work presented so far shows the efficiency of a blind search for a redshift by means of the X-ray spectral analysis of known clusters observed by Chandra. On the basis of these results, we can define general criteria for measuring accurate redshifts when applying this procedure to a sample of new clusters, whose redshift is not known. We can apply this to new extended sources detected in the Chandra and XMM archives. However, serendipitous searches in Chandra and XMM pointings, which are inevitably confined to relatively small sky areas, result in detections with a limited amount of net counts, such as the ChaMP Galaxy Cluster Survey (Barkhouse et al. 2006), the XMM-Newton Distant Cluster Project (XDCP, Fassbender 2008), the XMM-Newton Large-Scale Structure (XMM-LSS, Pierre et al. 2007), and the XMM Clusters Survey (XCS, Romer et al. 2001; Lloyd-Davies et al. 2010). In this case, the application of our procedure will still be helpful but have a modest impact.

The situation radically changes if we consider future X-ray surveys. The planned eROSITA satellite (Predehl et al. 2010; Cappelluti et al. 2010) and the proposed WFT mission (Murray & WFT Team 2010) will provide a large number of new detections. We focus here on specific expectations for WFT, which is the most optimized mission for surveys thanks to its wide-field optical design. This mission will be able to provide a golden sample of 15000-20000 rich clusters, with

$kT > 3$ keV out to $z \sim 1.5$, detected with more than 1500 counts (Borgani et al. 2010).

5.1. Selecting clusters with reliable z_X

We use the simulations we performed to assess WFXT science cases as described in Tozzi et al. (2010). Using the halo mass function by Sheth & Tormen (1999), we first determine the cosmological parameters that most accurately fit the observed X-ray cluster luminosity function (XLF, see Rosati et al. 1998; Giacconi et al. 2002; Bauer et al. 2002) for a given relation between cluster mass and X-ray luminosity. In this way, we can extrapolate the observed XLF over the luminosity and redshift ranges expected to be covered by the WFXT surveys. This luminosity function is then used to generate mock realizations of the WFXT cluster surveys through a Monte-Carlo procedure. The corresponding virial temperature (temperature gradients are not considered) is assigned with a scatter of 10% with respect to the mass, and the luminosity with a scatter of 15% - 45% (going from massive clusters to groups) with respect to the temperature, to be consistent with the observed L - T relation of local clusters. We are thus able to simulate an accurate spectrum normalized to the predicted flux of each cluster. Metal abundances are assigned randomly with a Gaussian distribution centered around the average value $Z = 0.3Z_\odot$ with a sigma $\Delta Z = 0.1Z_\odot$, with a hard lower limit at $Z = 0.1Z_\odot$. Values below $Z = 0.1Z_\odot$ have never been measured in hot clusters at any redshift. In addition, stacked spectra analyses of distant clusters identify significant enrichment in the ICM up to $z \sim 1.3$ (Balestra et al. 2007; Maughan et al. 2008). As a matter of fact, a safe assumption would be a constant Fe abundance equal to $0.3Z_\odot$, as also suggested by Figure 7. However, we believe that by allowing Z_{Fe} values as low as $0.1Z_\odot$, we will provide a conservative estimate of the number of line detections. We also note that with this choice, in the simulation analysis we obtain several best-fit values of the Z_{Fe} parameter populating the range below $0.1Z_\odot$. At present, it is impossible to provide a more accurate model for the distribution of Z_{Fe} in the ICM as a function of redshift.

The background is computed accordingly to expectations for the WFXT mission. The net count rates per deg^2 of the different background components are given in Table 4. We assume that the source spectrum is extracted from a 500 kpc region, a value calibrated on the analysis of real Chandra data as in Balestra et al. (2007). We also take into account that typically 10% of the total emitted flux is lost outside the extraction regions. The effect of vignetting is also considered, since the clusters will be randomly positioned across the field of view. This is an important factor to be included because the vignetting is particularly severe in the hard band, where the Fe line is located. We use effective area files corresponding to seven different off-axis angles in the range 0-30' to reproduce as closely as possible the vignetting effect on the observed spectra.

We produce a mock catalog of groups (with temperatures above 0.5 keV) and clusters as expected in 100 square degrees of the WFXT Medium Survey (see Rosati et al. 2010). The simulation thus consists of 100 pointings of 13.2 ks each, extracted from a total 3000 square degree area. We have about 2500 groups and clusters above the flux of 4×10^{-15} erg s $^{-1}$ cm 2 . For all of them, we measure the redshift z_X with our procedure described in Section 3. We remark that this mock sample, being flux limited, includes a large number of clusters with $kT \leq 2$ keV, for which the presence of the L-shell line complex at low energy significantly facilitates the measurement of z_X .

Background component	0.5-2 keV	2-7 keV
Particles	0.188	0.397
Galactic	21.4	0.0
AGN (Medium survey)	3.9	1.65
Cluster (Medium survey)	0.79	0.14
Total (Medium survey)	26.28	2.19

Table 4: WFXT background net count rates per deg^2 in the Medium Survey (13.2 ks exposure). The AGN and cluster contributions correspond to the emission of the unresolved AGN and groups/clusters, respectively, in the Medium Survey.

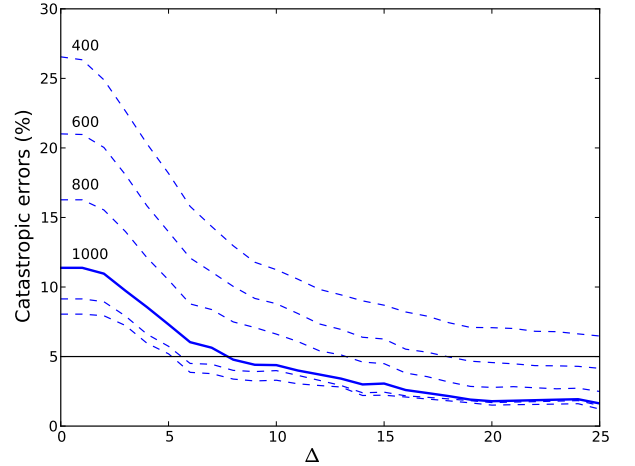


Fig. 14: Percentage of catastrophic errors as a function of ΔC_{stat} in a sample with different net photons within R_s from top to bottom. The horizontal line marks the 5% level.

The catastrophic errors are identified by means of 3σ clipping. In Figure 14, we plot the percentage of catastrophic failures as a function of ΔC_{stat} for clusters detected above a given photon threshold. We see that, for a given ΔC_{stat} , the number of catastrophic failures rapidly increases below 1000 net photons. By selecting a reference sample with more than 1000 net photons and $\Delta C_{stat} > 9$, we are able to maintain the percentage of catastrophic errors below 5%. The effect of the criterion $\Delta C_{stat} > 9$ can be appreciated by comparing Figs 15 and 16. In Fig. 15, we show all the groups and clusters with more than 1000 net photons, while in Fig. 16 we apply the threshold $\Delta C_{stat} > 9$, which helps to define a “golden” sample of 862 groups and clusters. This sample still includes 38 catastrophic errors (4.4% of the total) but all of them are rejected marginally with redshift deviations slightly larger than 0.032. After applying the cut for $\Delta C_{stat} > 9$, the mean redshift offset $\langle \Delta z \rangle$ is -0.0024 and the deviation rms Δz_{rms} is 0.0116 (see Figure 17). We note that, despite 38 measurements being classified as catastrophic errors, their typical discrepancy is still very small, and the overall redshift accuracy of the sample with $\Delta C_{stat} > 9$ satisfies the demands of cosmological tests. For example, in order not to degrade dark energy constraints by more than 10%, both $\langle \Delta z \rangle < 0.003$ and $\Delta z_{rms} < 0.03$ are required (Lima & Hu 2007), which are satisfied by our “golden” sample.

Figure 18 shows $\Delta z = z_X - z_o$ as a function of ΔC_{stat} for all the clusters with detections of more than 1000 photons. The error rapidly decreases with increasing ΔC_{stat} , as expected. The relation between Δz_{rms} and ΔC_{stat} can be approximated as

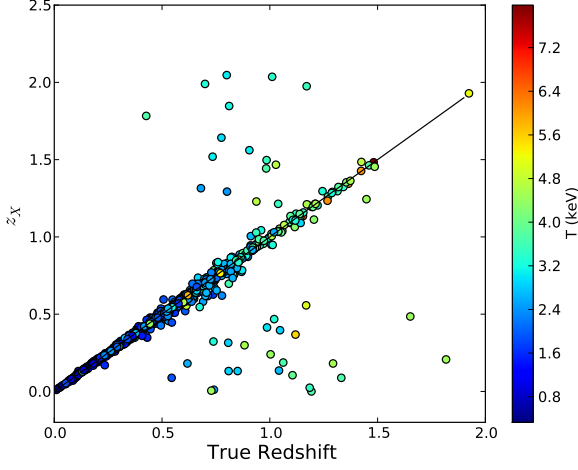


Fig. 15: X-ray measured redshift z_X for all the clusters in a 100 square degree field of the WFXT Medium Survey detected with more than 1000 photons within the extraction region. We have 1037 clusters and groups, and 118 catastrophic failures. The colors are set according to the cluster temperature.

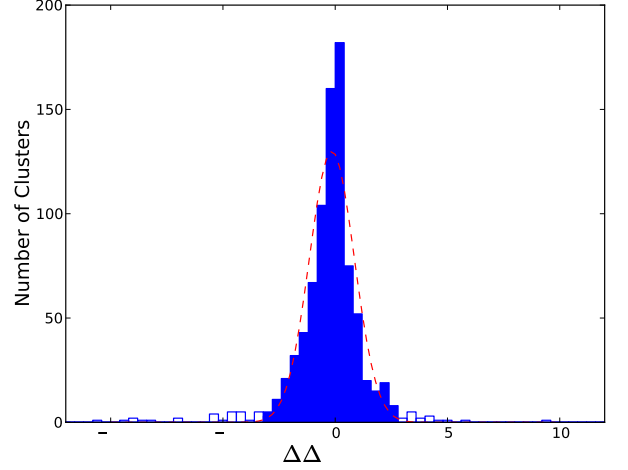


Fig. 17: Histogram of $\Delta z / \Delta z_{rms}$ from a simulated 100 square degrees of the WFXT Medium Survey. The sample here include all clusters with more than 1000 photons and ΔC_{stat} larger than 9. Empty histogram indicates the residual catastrophic errors. The red dashed line shows the Gaussian fit after 3σ clipping.

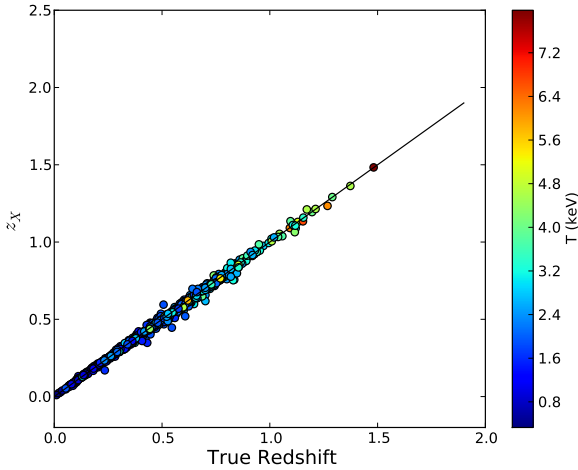


Fig. 16: The same as Figure 15, but after applying the criterion $\Delta C_{stat} > 9$. There are no deviations larger than 0.1, and only 38 clusters with $\Delta z > 0.032$. The size of the sample has decreased to 862.

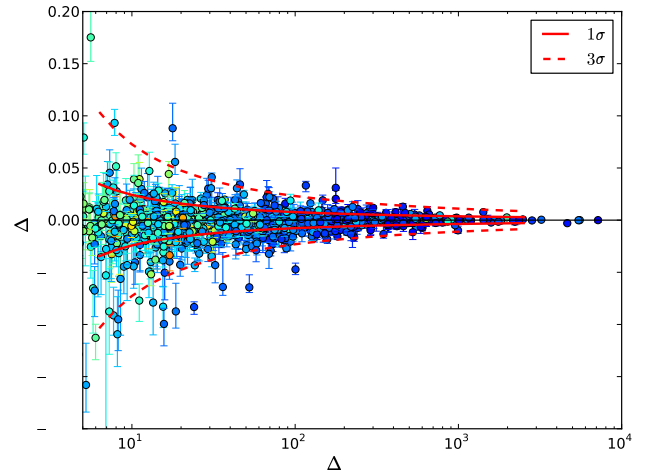


Fig. 18: $\Delta z = z_X - z_o$ versus ΔC_{stat} for clusters with more than 1000 photons. Error bars show 1σ statistical error from XSPEC fitting. The color code is the same as in Figure 15. There is an obvious trend of Δz decreasing at larger ΔC_{stat} . The red solid lines delineate 1σ envelope for Δz_{rms} . The red dashed lines delineate the 3σ confidence levels.

$$\Delta z_{rms} = 0.025(\log_{10} \Delta C_{stat})^{-1.5}. \quad (2)$$

With this information we can select a sample with reliable redshifts and a robust error estimate for z_X .

5.2. Assessing the completeness of the sample

Samples selected with source counts above a given number of net photons can still be treated as "complete". Such a threshold corresponds to a good accuracy for the limiting flux as a function of the position on the sky, once the exposure time and the vignetting in each field of view is computed. Therefore, it is possible to obtain a clearly defined sky coverage from which the

XLF and the X-ray Temperature Function (XTF) can be computed for cosmological applications.

However, it is clear that a criterion based solely on the net counts is an insufficient one. As is immediately visible from Figure 15, among the clusters whose X-ray spectra have more than 1000 photons, there are about 120 catastrophic failures, several of which are at a redshift much higher than the true one. This implies that there may be a significant contamination at the bright ends of the luminosity and temperature functions, which are both particularly sensitive to cosmological parameters. For example, six clusters in our sample with more than 1500 counts are incorrectly located at $z > 1.5$. For the full

3000 deg² Medium Survey, this would correspond to about 180 fake $z > 1.5$ clusters, compared to the 20 expected (see Figure 2 in Borgani et al. 2010). This implies that the majority of the rarest $z > 1.5$ clusters candidates would be spurious, and therefore that the constraints on both cosmological parameters and non-Gaussianity (e.g. Sartoris et al. 2010; Verde 2010, and references therein) would be highly biased without applying the $\Delta C_{stat} > 9$ criterion.

By adopting the threshold on ΔC_{stat} , the price to pay is a lower level of completeness of the sample. In the aforementioned simulation, we have excluded 175 clusters (17% of the total) detected with a number of photons above the threshold because they do not satisfy the $\Delta C_{stat} > 9$ criterion. In this way, we remove most of the catastrophic errors but also lose about 100 clusters with a good z_X . As a result, the “golden sample” is incomplete above a given flux threshold, and the missing clusters must be accounted before applying cosmological tests. Unfortunately, this step is difficult because the temperature distribution of the clusters with $\Delta C_{stat} < 9$ is biased with respect to the distribution of the entire sample. This is shown in Figure 19, where the normalized distribution of rejected clusters with more than 1000 photons is skewed towards high temperatures. This occurs because it is generally more difficult to fit the Fe line in increasingly hot clusters, since the abundance of He-like Fe ions, which dominate the line emission, begins to decrease at temperatures $kT > 5$ keV, and the thermal continuum steadily increases. Such a bias against the most massive objects needs to be carefully quantified.

There are two ways to restore the completeness of the sample. One is to statistically correct the incompleteness using results from N-body simulations. However, this is affected by serious systematic errors because we modify the high-mass end of the cluster distribution, which is the most sensitive to cosmological parameters. The other option is to limit spectroscopic follow-up to only those clusters with $\Delta C_{stat} < 9$.

To design the optimal strategy, we should proceed with a detailed investigation of the effects of varying the threshold of ΔC_{stat} on the cosmological parameter constraints. We noted in Section 5.1 that $\Delta C_{stat} > 9$ provide a “golden sample” that largely satisfies the requirements of achieving a precision of 10% for the dark energy constraints. Relaxing the threshold on ΔC_{stat} and mapping the threshold values to the accuracy on the cosmological parameter is clearly an option that we plan to explore in a future paper.

Another possible source of contamination may be diffuse X-ray emissions produced by inverse Compton processes associated with radio jets (see, for example, Fabian et al. 2003). These sources are a serious contaminant when detecting X-ray extended sources, especially at very low fluxes. However, this source will hardly provide a spurious line detection above the selection threshold, hence their presence in a cosmological “golden” sample can be neglected.

6. Conclusions

We have performed a blind search of the Fe line in the X-ray spectra of clusters of galaxies using Chandra archival data. Our goal is to define the optimal methodology for determining X-ray redshifts and to quantify their accuracy by investigating both statistical and systematic errors. To this end, we compared z_X with the value z_o determined with optical spectroscopic observations.

We have found good agreement in general, but also in several cases where z_X is determined by the false detection of

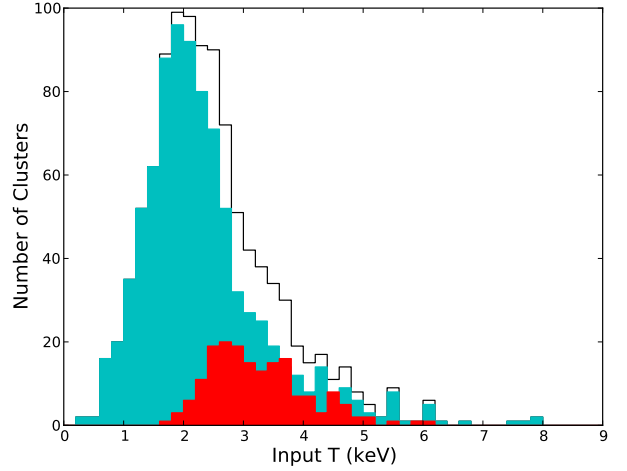


Fig. 19: Temperature distribution for the sample of groups and clusters detected with more than 1000 net photons and $\Delta C_{stat} > 9$ (filled histogram). The black line indicates the complete input catalog, while the red histogram refers to the clusters removed from the flux-limited sample after applying the criterion $\Delta C_{stat} > 9$.

an emission line. Thus we explored different methods to minimize the number of these catastrophic failures. We have found that it is preferable to use the total available band (0.5-7 keV) for both selecting the extraction region and fitting the spectra. Catastrophic failures are found to be caused by low spectrum S/N and an intrinsically low Fe abundance. For this reason, a lower limit to the net detected photons is insufficient to guarantee a robust measurement of the redshift. However, we find that we can exclude most catastrophic errors by using the criterion $\Delta C_{stat} > 9$, where ΔC_{stat} is the difference between the best-fit value of C_{stat} , and its best-fit value when the metal abundance is constrained to be zero.

We have also explored the use of weak priors to improve the results. We have found that by fixing the Fe abundance to the local average value $Z_{Fe} = 0.3Z_{\odot}$, the number of catastrophic errors is not reduced. Furthermore, by requiring that all the fitted clusters agree with the observed local L - T relation and its scatter, one has an independent method to identify outliers, although not as efficiently as the condition $\Delta C_{stat} > 9$.

Our spectral analysis of Chandra clusters shows that future X-ray survey missions will be able to define sizable samples of clusters with X-ray measured redshifts. We specifically investigated the case of the Wide Field X-ray Telescope using a mock catalog of ~ 2500 groups and clusters extracted from a 100 square degree area of the WFT Medium Survey. The input cluster catalog is generated from the cluster mass function normalized to the observed space density of X-ray clusters by assuming local scaling relations to derive X-ray luminosities and temperatures associated with a given mass. We found that, by applying the condition $\Delta C_{stat} > 9$, we can successfully measure the redshift of 862 clusters with more than 1000 net counts, which leaves a small fraction (4.4%) of marginally catastrophic errors. We argue that these subsamples with X-ray determined redshifts can be effectively used for cosmological applications, thus avoiding time-consuming spectroscopic observations, although additional simulations will have to be developed to assess the completeness of the sample down to a given flux limit.

Acknowledgements. We thank Stefano Ettori for helpful discussions, Sergio Campana, Paolo Conconi, and Andy Ptak for providing the WFXT response files. We also thank the anonymous referee for insightful comments and suggestions. We acknowledge financial contribution from contract ASI-INAF I/088/06/0, from the PD51 INFN grant, and from the PRIN-MIUR grant "The cosmic cycle of baryons". The work is also supported by the National Science Foundation of China under the Distinguished Young Scholar Grant 10825313 the Ministry of Science and Technology national basic science Program (Project 973) under grant No. 2007CB815401, and the Fundamental Research Funds for the Central Universities. HY acknowledges the support of ICTP-IAEA Sandwich Training Educational Programme (STEP), and of the China Scholarship Council.

References

- Allen, S. W., Schmidt, R. W., Ebeling, H., Fabian, A. C., & van Speybroeck, L. 2004, *MNRAS*, 353, 457 [1](#)
- Anders, E. & Grevesse, N. 1989, *Geochim. Cosmochim. Acta*, 53, 197 [2](#), [3](#), [1](#)
- Arnaud, K. A. 1996, in *Astronomical Society of the Pacific Conference Series*, Vol. 101, *Astronomical Data Analysis Software and Systems V*, ed. G. H. Jacoby & J. Barnes, 17–+ [2](#)
- Balestra, I., Tozzi, P., Ettori, S., et al. 2007, *A&A*, 462, 429 [1](#), [2](#), [4](#), [1](#), [5](#), [1](#)
- Barkhouse, W. A., Green, P. J., Vikhlinin, A., et al. 2006, *ApJ*, 645, 955 [5](#)
- Bauer, F. E., Alexander, D. M., Brandt, W. N., et al. 2002, *AJ*, 124, 2351 [5](#), [1](#)
- Baumgartner, W. H., Loewenstein, M., Horner, D. J., & Mushotzky, R. F. 2005, *ApJ*, 620, 680 [4](#), [1](#)
- Böhringer, H., Voges, W., Huchra, J. P., et al. 2000, *ApJS*, 129, 435 [1](#)
- Böhringer, H. & Werner, N. 2010, *A&A Rev.*, 18, 127 [1](#)
- Borgani, S. 2006, *ArXiv:astro-ph/0605575* [1](#)
- Borgani, S. & Guzzo, L. 2001, *Nature*, 409, 39 [1](#)
- Borgani, S., Rosati, P., Sartoris, B., Tozzi, P., & Giacconi, R. 2010, *ArXiv:1010.6213* [5](#), [5](#), [2](#)
- Braito, V., Maccacaro, T., Caccianiga, A., Severgnini, P., & Della Ceca, R. 2005, *ApJ*, 621, L97 [1](#)
- Branchesi, M., Gioia, I. M., Fanti, C., & Fanti, R. 2007, *A&A*, 472, 739 [4](#), [2](#)
- Caccianiga, A., Maccacaro, T., Wolter, A., Della Ceca, R., & Gioia, I. M. 2000, *A&AS*, 144, 247 [1](#)
- Cappelluti, N., Predehl, P., Böhringer, H., et al. 2010, *ArXiv:1004.5219* [5](#)
- Cash, W. 1979, *ApJ*, 228, 939 [3](#), [1](#)
- Cavaliere, A. & Fusco-Femiano, R. 1976, *A&A*, 49, 137 [3](#), [1](#)
- Ebeling, H., Barrett, E., Donovan, D., et al. 2007, *ApJ*, 661, L33 [1](#)
- Ebeling, H., Edge, A. C., Mantz, A., et al. 2010, *ArXiv:1004.4683* [1](#)
- Ebeling, H., Jones, L. R., Fairley, B. W., et al. 2001, *ApJ*, 548, L23 [1](#)
- Ettori, S., Tozzi, P., Borgani, S., & Rosati, P. 2004, *A&A*, 417, 13 [1](#), [4](#), [2](#)
- Fabian, A. C., Sanders, J. S., Crawford, C. S., & Ettori, S. 2003, *MNRAS*, 341, 729 [5](#), [2](#)
- Fassbender, R. 2008, *ArXiv:0806.0861* [5](#)
- Giacconi, R., Zirm, A., Wang, J., et al. 2002, *ApJS*, 139, 369 [5](#), [1](#)
- Gioia, I. M. & Luppino, G. A. 1994, *ApJS*, 94, 583 [1](#)
- Hashimoto, Y., Barcons, X., Böhringer, H., et al. 2004, *A&A*, 417, 819 [1](#)
- Henry, J. P., Gioia, I. M., Mullis, C. R., et al. 1997, *AJ*, 114, 1293 [1](#)
- Holden, B. P., Stanford, S. A., Squires, G. K., et al. 2002, *AJ*, 124, 33 [1](#)
- Kaastra, J. 1992, *An X-Ray Spectral Code for Optically Thin Plasmas* (Internal SRONLeiden Report, updated version 2.0) [2](#)
- Kalberla, P. M. W., Burton, W. B., Hartmann, D., et al. 2005, *A&A*, 440, 775 [1](#)
- Komatsu, E., Smith, K. M., Dunkley, J., et al. 2010, *ArXiv:1001.4538* [1](#)
- Kotov, O. & Vikhlinin, A. 2006, *ApJ*, 641, 752 [1](#)
- Lamer, G., Hoeft, M., Kohnert, J., Schwöpe, A., & Storm, J. 2008, *A&A*, 487, L33 [1](#)
- Lewis, A. D., Ellingson, E., Morris, S. L., & Carlberg, R. G. 1999, *ApJ*, 517, 587 [1](#)
- Liedahl, D. A., Osterheld, A. L., & Goldstein, W. H. 1995, *ApJ*, 438, L115 [2](#)
- Lima, M. & Hu, W. 2007, *Phys. Rev. D*, 76, 123013 [5](#), [1](#)
- Lloyd-Davies, E. J., Romer, A. K., Hosmer, M., et al. 2010, *ArXiv:1010.0677* [5](#)
- Lumb, D. H., Bartlett, J. G., Romer, A. K., et al. 2004, *A&A*, 420, 853 [4](#), [2](#)
- Maccacaro, T., Braito, V., Della Ceca, R., Severgnini, P., & Caccianiga, A. 2004, *ApJ*, 617, L33 [1](#)
- Mantz, A., Allen, S. W., Rapetti, D., & Ebeling, H. 2010, *MNRAS*, 406, 1759 [1](#)
- Martini, P., Mulchaey, J. S., & Kelson, D. D. 2007, *ApJ*, 664, 761 [1](#)
- Maughan, B. J., Jones, C., Forman, W., & Van Speybroeck, L. 2008, *ApJS*, 174, 117 [1](#), [5](#), [1](#)
- Maughan, B. J., Jones, L. R., Ebeling, H., & Scharf, C. 2006, *MNRAS*, 365, 509 [4](#), [2](#), [13](#), [4](#), [2](#)
- Mewe, R., Gronenschild, E. H. B. M., & van den Oord, G. H. J. 1985, *A&AS*, 62, 197 [2](#)
- Mewe, R., Lemen, J. R., & van den Oord, G. H. J. 1986, *A&AS*, 65, 511 [2](#)
- Mitchell, R. J., Culhane, J. L., Davison, P. J. N., & Ives, J. C. 1976, *MNRAS*, 175, 29P [1](#)
- Moran, S. M., Ellis, R. S., Treu, T., et al. 2007, *ApJ*, 671, 1503 [1](#)
- Mullis, C. R., McNamara, B. R., Quintana, H., et al. 2003, *ApJ*, 594, 154 [1](#)
- Mullis, C. R., Rosati, P., Lamer, G., et al. 2005, *ApJ*, 623, L85 [1](#)
- Murray, S. S. & WFXT Team. 2010, in *Bulletin of the American Astronomical Society*, Vol. 42, *Bulletin of the American Astronomical Society*, 520–+ [1](#), [5](#)
- Mushotzky, R. F. & Loewenstein, M. 1997, *ApJ*, 481, L63+ [1](#)
- Nousek, J. A. & Shue, D. R. 1989, *ApJ*, 342, 1207 [3](#), [1](#)
- Perlman, E. S., Horner, D. J., Jones, L. R., et al. 2002, *ApJS*, 140, 265 [1](#)
- Pierre, M., Chiappetti, L., Pacaud, F., et al. 2007, *MNRAS*, 382, 279 [5](#)
- Pratt, G. W., Croston, J. H., Arnaud, M., & Böhringer, H. 2009, *A&A*, 498, 361 [4](#), [2](#)
- Predehl, P., Böhringer, H., Brunner, H., et al. 2010, in *American Institute of Physics Conference Series*, Vol. 1248, *American Institute of Physics Conference Series*, ed. A. Comastri, L. Angelini, & M. Cappi, 543–548 [1](#), [5](#)
- Rasmussen, J. & Ponman, T. J. 2007, *MNRAS*, 380, 1554 [4](#), [1](#)
- Renzini, A. 1997, *ApJ*, 488, 35 [4](#), [1](#)
- Romer, A. K., Viana, P. T. P., Liddle, A. R., & Mann, R. G. 2001, *Astrophys. J.*, 547, 594 [5](#)
- Rosati, P., Borgani, S., Gilli, R., et al. 2010, *ArXiv:1010.6252* [1](#), [5](#), [1](#)
- Rosati, P., Borgani, S., & Norman, C. 2002, *ARA&A*, 40, 539 [1](#)
- Rosati, P., della Ceca, R., Norman, C., & Giacconi, R. 1998, *ApJ*, 492, L21+ [5](#), [1](#)
- Rosati, P., Stanford, S. A., Eisenhardt, P. R., et al. 1999, *AJ*, 118, 76 [1](#)
- Rosati, P., Tozzi, P., Ettori, S., et al. 2004, *AJ*, 127, 230 [1](#), [1](#)
- Rosati, P., Tozzi, P., Gobat, R., et al. 2009, *A&A*, 508, 583 [1](#)
- Sartoris, B., Borgani, S., Fedeli, C., et al. 2010, *MNRAS*, 407, 2339 [5](#), [2](#)
- Schuecker, P. 2005, in *Reviews in Modern Astronomy*, Vol. 18, *Reviews in Modern Astronomy*, ed. S. Röser, 76–105 [1](#)
- Sheth, R. & Tormen, G. 1999, *Monthly Notices of the Royal Astronomical Society*, 308, 119 [5](#), [1](#)
- Stanford, S. A., Eisenhardt, P. R., Brodwin, M., et al. 2005, *ApJ*, 634, L129 [1](#)
- Stanford, S. A., Holden, B., Rosati, P., et al. 2002, *AJ*, 123, 619 [1](#)
- Stoeckle, J. T., Morris, S. L., Gioia, I. M., et al. 1991, *ApJS*, 76, 813 [1](#)
- Struble, M. F. & Rood, H. J. 1999, *ApJS*, 125, 35 [1](#)
- Tozzi, P. 2007, in *Lecture Notes in Physics*, Berlin Springer Verlag, Vol. 720, *The Invisible Universe: Dark Matter and Dark Energy*, ed. L. Papantonopoulos, 125–+ [1](#)
- Tozzi, P., Rosati, P., Ettori, S., et al. 2003, *ApJ*, 593, 705 [1](#)
- Tozzi, P., Santos, J., Yu, H., et al. 2010, *ArXiv:1010.6208* [5](#), [1](#)
- Tran, K., Franx, M., Illingworth, G. D., et al. 2007, *ApJ*, 661, 750 [1](#)
- Tucker, W., Blanco, P., Rappoport, S., et al. 1998, *ApJ*, 496, L5+ [1](#)
- Verde, L. 2010, *Advances in Astronomy*, 2010 [5](#), [2](#)
- Vikhlinin, A., Kravtsov, A. V., Burenin, R. A., et al. 2009, *ApJ*, 692, 1060 [1](#)
- Vikhlinin, A., Markevitch, M., Murray, S. S., et al. 2005, *ApJ*, 628, 655 [1](#)
- Vikhlinin, A., McNamara, B. R., Forman, W., et al. 1998, *ApJ*, 502, 558 [1](#)
- Voit, G. M. 2005, *Rev. Mod. Phys.*, 77, 207 [1](#)
- Wilms, J., Allen, A., & McCray, R. 2000, *ApJ*, 542, 914 [2](#)

ID	z_o	ref	ObsID	Detector/Mode	$t_{exp}(ks)$	$T(z_o)(keV)$	$Z_{Fe}(z_o)/Z_{\odot}$	$nH(cm^{-2})$
Abell907	0.160	1	3185	I-V	47	$5.56^{+0.09}_{-0.09}$	$0.49^{+0.04}_{-0.04}$	5.65×10^{20}
Abell1689	0.187	2	540,1663	I-F	21	$13.74^{+0.65}_{-0.65}$	$0.34^{+0.07}_{-0.07}$	1.82×10^{20}
1E0657-56	0.296	3	554	I-F	25	$13.17^{+0.63}_{-0.63}$	$0.2^{+0.06}_{-0.06}$	6.5×10^{20}
MS1008.1-1224	0.306	4	926	I-V	44	$6.09^{+0.32}_{-0.32}$	$0.27^{+0.06}_{-0.06}$	7.26×10^{20}
MS2137.3-2353	0.313	5	928	S-V	34	$5.26^{+0.33}_{-0.33}$	$0.35^{+0.04}_{-0.04}$	3.55×10^{20}
Abell1995	0.319	6	906	S-F	56.4	$9.13^{+0.32}_{-0.31}$	$0.4^{+0.07}_{-0.07}$	1.42×10^{20}
ZwCl1358.1+6245	0.328	8	516	S-F	48.3	$7.12^{+0.26}_{-0.25}$	$0.39^{+0.07}_{-0.07}$	1.92×10^{20}
MACSJ0404.6+1109	0.355	9	3269	I-V	21.6	$6.9^{+0.6}_{-0.8}$	$0.16^{+0.07}_{-0.11}$	1.43×10^{20}
RXJ0027.6+2616	0.367	9	3249	I-V	9.8	$8.07^{+1.73}_{-1.39}$	$0.52^{+0.30}_{-0.24}$	3.86×10^{20}
MACSJ1720.2+3536	0.387	10	3280	I-V	20.8	$6.54^{+0.35}_{-0.34}$	$0.45^{+0.08}_{-0.08}$	3.4×10^{20}
ZwCl0024.0+1652	0.395	11	929	S-F	39.5	$4.57^{+0.49}_{-0.27}$	$0.75^{+0.21}_{-0.18}$	4.23×10^{20}
RXJ1416.4+4446	0.400	12	541	I-V	31	$3.56^{+0.2}_{-0.19}$	$0.86^{+0.25}_{-0.21}$	1.22×10^{20}
MACSJ0159.8-0849	0.405	13	3265	I-V	17.6	$9.53^{+0.74}_{-0.5}$	$0.35^{+0.08}_{-0.08}$	2.08×10^{20}
MACSJ2228.5+2036	0.412	9	3285	I-V	20	$8.25^{+0.61}_{-0.6}$	$0.35^{+0.09}_{-0.09}$	4.58×10^{20}
MS0302.7+1658	0.424	8	525	I-V	10	$4.38^{+0.61}_{-0.45}$	$0.45^{+0.24}_{-0.19}$	10.9×10^{20}
MACSJ0417.5-1154	0.44	14	3270	I-V	12	$12.48^{+1.24}_{-1.06}$	$0.29^{+0.11}_{-0.11}$	3.86×10^{20}
MACSJ1206.2-0847	0.44	15	3277	I-V	23	$12.61^{+0.97}_{-0.88}$	$0.17^{+0.08}_{-0.08}$	3.72×10^{20}
RXJ1701.3+6414	0.453	16	547	I-V	49	$4.49^{+0.3}_{-0.26}$	$0.51^{+0.13}_{-0.06}$	2.46×10^{20}
RXJ1641.8+4001	0.464	16	3575	I-V	45	$4.81^{+0.62}_{-0.54}$	$0.48^{+0.21}_{-0.17}$	1.1×10^{20}
MACSJ1824.3+4309	0.483	10	3255	I-V	14.8	$8.94^{+2.57}_{-2.26}$	< 0.23	4.58×10^{20}
MACSJ1311.0-0311	0.494	17	3258	I-V	14.8	$8.67^{+0.98}_{-0.91}$	$0.37^{+0.15}_{-0.14}$	1.87×10^{20}
RXJ1524.6+0957	0.516	16	1664	I-V	50	$5.58^{+0.59}_{-0.48}$	$0.34^{+0.14}_{-0.12}$	2.91×10^{20}
MS0015.9+1609	0.541	8	520	I-V	67	$8.3^{+0.32}_{-0.32}$	$0.31^{+0.05}_{-0.05}$	7.26×10^{20}
MACSJ1423.8+2404	0.543	18	1657	I-V	18.5	$7.61^{+0.68}_{-0.52}$	$0.3^{+0.1}_{-0.09}$	2.38×10^{20}
MACSJ1149.5+2223	0.544	18	1656, 3589	I-V	38	$12.75^{+1.17}_{-0.97}$	$0.27^{+0.1}_{-0.1}$	2.28×10^{20}
SC1120-1202	0.562	7	3235	I-V	68	$6.49^{+1.35}_{-1.11}$	$0.21^{+0.23}_{-0.19}$	5.19×10^{20}
MS2053.7-0449	0.583	8	551, 1667	I-V	88	$6.94^{+0.67}_{-0.62}$	$0.18^{+0.12}_{-0.1}$	4.96×10^{20}
RXJ0956.0+4107	0.587	16	5294	I-V	17.2	$8.19^{+2.78}_{-1.79}$	$0.18^{+0.32}_{-0.18}$	1.14×10^{20}
MACSJ2129.4-0741	0.589	18	3199	I-V	17.6	$9.48^{+1.25}_{-0.8}$	$0.54^{+0.15}_{-0.14}$	4.86×10^{20}
MACSJ0647.7+7015	0.591	18	3196	I-V	19.2	$12.10^{+1.54}_{-1.08}$	< 0.1	5.64×10^{20}
RXJ0542.8-4100	0.634	7	914	I-F	50	$7.93^{+1.1}_{-0.85}$	$0.18^{+0.14}_{-0.12}$	3.73×10^{20}
MACSJ0744.9+3927	0.698	18	3197, 3585	I-V	40	$9.51^{+0.77}_{-0.54}$	$0.29^{+0.09}_{-0.08}$	5.7×10^{20}
RXJ1221.4+4918	0.70	12	1662	I-V	78	$9.2^{+1.06}_{-0.83}$	$0.29^{+0.14}_{-0.12}$	1.47×10^{20}
RXJ2302.8+0844	0.722	19	918	I-F	108	$7.35^{+1.22}_{-0.85}$	$0.17^{+0.17}_{-0.15}$	4.91×10^{20}
RXJ1113.1-2615	0.725	19	915	I-F	103	$6.41^{+0.89}_{-0.82}$	$0.35^{+0.19}_{-0.17}$	5.48×10^{20}
MS1137.5+6624	0.782	20	536	I-V	117	$7.33^{+0.58}_{-0.51}$	$0.24^{+0.12}_{-0.11}$	1.2×10^{20}
RXJ1350.0+6007	0.804	21	2229	I-V	58	$4.38^{+0.76}_{-0.57}$	$0.57^{+0.34}_{-0.26}$	1.78×10^{20}
RXJ1317.4+2911	0.805	21	2228	I-V	110.5	$3.77^{+1.09}_{-0.71}$	$0.48^{+0.55}_{-0.36}$	1.1×10^{20}
RXJ1716.4+6708	0.813	22	548	I-F	51	$6.57^{+0.72}_{-0.67}$	$0.57^{+0.14}_{-0.17}$	3.7×10^{20}
MS1054.4-0321	0.832	23	512	S-F	80	$7.26^{+0.44}_{-0.35}$	$0.23^{+0.07}_{-0.07}$	3.6×10^{20}
1WGAJ1226.9+3332	0.89	24	3180	I-V	31.5	$12.03^{+1.46}_{-1.17}$	< 0.11	1.38×10^{20}
CLJ1415.1+3612	1.013	19	4163	I-V	89	$6.76^{+0.74}_{-0.67}$	$0.32^{+0.16}_{-0.14}$	1.09×10^{20}
RXJ0910+5422	1.106	25	2227, 2452	I-V	170	$5.85^{+1.59}_{-1.08}$	$0.08^{+0.26}_{-0.08}$	2.2×10^{20}
RXJ1252-2927	1.235	27	4198, 4403	I-V	188.4	$6.81^{+1.24}_{-0.87}$	$0.84^{+0.32}_{-0.27}$	5.95×10^{20}
RXJ0848.9+4452	1.261	26	927, 1708	I-V	184.5	$4.44^{+1.11}_{-0.86}$	$0.37^{+0.47}_{-0.29}$	2.6×10^{20}
XMMUJ2235.3-2557	1.393	28	6975/6, 7367/8, 7404	S-V	196	$9.96^{+1.6}_{-1.28}$	$0.41^{+0.24}_{-0.21}$	1.47×10^{20}

Table 1: The cluster sample used in this work, in order of increasing redshift. We show the properties of each data-set, including the references to previously published works, observation ID, detector (I=ACIS-I, S=ACIS-S), observation mode (F=FAINT, V=VERYFAINT), and exposure time. The best-fit parameters $T(z_o)$ and $Z_{Fe}(z_o)$ are obtained with the redshift frozen to the optical value z_o . Temperature and metal abundance refer to the global fit to the spectrum extracted within the radius R_{ext} , and therefore represents an average value whenever a temperature or a metallicity gradient is present. The last column refers to the Galactic Hydrogen column density as measured by [Kalberla et al. \(2005\)](#).

References. (1):[Vikhlinin et al. \(2005\)](#); (2):[Martini et al. \(2007\)](#); (3):[Tucker et al. \(1998\)](#); (4):[Lewis et al. \(1999\)](#); (5):[Mushotzky & Loewenstein \(1997\)](#); (6):[Struble & Rood \(1999\)](#); (7):[Balestra et al. \(2007\)](#); (8):[Stoeckel et al. \(1991\)](#); (9):[Böhringer et al. \(2000\)](#); (10):[Ebeling et al. \(2010\)](#); (11):[Moran et al. \(2007\)](#); (12):[Vikhlinin et al. \(1998\)](#); (13):[Kotov & Vikhlinin \(2006\)](#); (14):[Caccianiga et al. \(2000\)](#); (15):[Borgani & Guzzo \(2001\)](#); (16):[Mullis et al. \(2003\)](#); (17):[Allen et al. \(2004\)](#); (18):[Ebeling et al. \(2007\)](#); (19):[Perlman et al. \(2002\)](#); (20):[Gioia & Luppino \(1994\)](#); (21):[Holden et al. \(2002\)](#); (22):[Henry et al. \(1997\)](#); (23):[Tran et al. \(2007\)](#); (24):[Ebeling et al. \(2001\)](#); (25):[Stanford et al. \(2002\)](#); (26):[Rosati et al. \(1999\)](#); (27):[Rosati et al. \(2004\)](#); (28):[Mullis et al. \(2005\)](#).

ID	z_o	z_X	$T(z_X)$ (keV)	$Z_{Fe}(z_X)/Z_\odot$	Cts (0.5-7 keV)	SN	$R_{ext}('')$	ΔC_{stat}
Abell907	0.160	$0.163^{+0.002}_{-0.002}$	$5.58^{+0.09}_{-0.1}$	$0.49^{+0.04}_{-0.04}$	48230 ± 238	202.5	162.4	220.56
Abell1689	0.187	$0.199^{+0.005}_{-0.005}$	$13.90^{+0.64}_{-0.65}$	$0.37^{+0.07}_{-0.07}$	34008 ± 200	170.3	93.5	31.59
1E0657-56	0.296	$0.325^{+0.006}_{-0.006}$	$13.3^{+0.63}_{-0.63}$	$0.26^{+0.05}_{-0.05}$	35384 ± 204	173.1	211.6	24.65
MS1008.1-1244	0.306	$0.3^{+0.014}_{-0.016}$	$6.05^{+0.37}_{-0.34}$	$0.27^{+0.06}_{-0.06}$	8993 ± 103	87.2	108.2	24.32
MS2137.3-2353	0.313	$0.313^{+0.002}_{-0.002}$	$5.26^{+0.11}_{-0.12}$	$0.35^{+0.04}_{-0.03}$	29509 ± 176	167.9	76.3	171.03
Abell1995	0.319	$0.313^{+0.003}_{-0.005}$	$9.05^{+0.32}_{-0.31}$	$0.41^{+0.07}_{-0.06}$	27217 ± 178	152.9	103.3	47.46
ZW1358.1+6245	0.328	$0.315^{+0.005}_{-0.003}$	$7.01^{+0.25}_{-0.26}$	$0.43^{+0.07}_{-0.07}$	18322 ± 149	123.2	88.6	51.1
MACSJ0404.6+1109	0.355	$2.146^{+0.052}_{-0.048}$	$44.51^{+12.38}_{-8.76}$	$3.09^{+2.46}_{-1.3}$	2368 ± 59	39.9	120.5	3.67
RXJ0027.6+2616	0.367	$0.373^{+0.024}_{-0.023}$	$8.08^{+1.19}_{-1.40}$	$0.514^{+0.29}_{-0.24}$	702 ± 31	22.7	81.2	5.15
MACSJ1720.2+3536	0.387	$0.385^{+0.005}_{-0.008}$	$6.51^{+0.35}_{-0.36}$	$0.45^{+0.08}_{-0.07}$	6370 ± 84	75.9	91.0	50.46
ZW0024.0+1652	0.395	$0.397^{+0.006}_{-0.005}$	$4.58^{+0.5}_{-0.27}$	$0.76^{+0.19}_{-0.17}$	2671 ± 59	45.3	59.0	29.0
RXJ1416.4+4446	0.400	$0.413^{+0.007}_{-0.016}$	$3.6^{+0.22}_{-0.19}$	$0.87^{+0.25}_{-0.21}$	2120 ± 51	41.9	76.3	31.91
MACSJ0159.8-0849	0.405	$0.406^{+0.01}_{-0.009}$	$9.54^{+0.75}_{-0.5}$	$0.35^{+0.08}_{-0.08}$	7852 ± 93	84.5	113.2	20.98
MACSJ2228.5+2036	0.412	$0.411^{+0.008}_{-0.009}$	$8.25^{+0.59}_{-0.58}$	$0.35^{+0.09}_{-0.08}$	6004 ± 86	69.4	137.8	18.47
MS0302.7+1658	0.424	$0.427^{+0.014}_{-0.014}$	$4.38^{+0.6}_{-0.44}$	$0.45^{+0.24}_{-0.19}$	652 ± 27	24.0	68.9	8.48
MACSJ0417.5-1154	0.44	$0.458^{+0.016}_{-0.011}$	$12.58^{+1.3}_{-1.04}$	$0.33^{+0.11}_{-0.11}$	7544 ± 95	79.4	132.8	9.84
MACSJ1206.2-0847	0.44	$0.403^{+0.014}_{-0.012}$	$11.79^{+1.07}_{-0.71}$	$0.22^{+0.08}_{-0.08}$	11267 ± 112	100.2	127.9	7.8
RXJ1701.3+6414	0.453	$0.454^{+0.008}_{-0.009}$	$4.49^{+0.31}_{-0.25}$	$0.51^{+0.13}_{-0.12}$	2731 ± 59	46.1	68.9	27.75
RXJ1641.8+4001	0.464	$0.45^{+0.008}_{-0.01}$	$4.64^{+0.64}_{-0.43}$	$0.54^{+0.22}_{-0.19}$	983 ± 35	28.4	46.7	12.91
MACSJ1824.3+4309	0.483	$0.368^{+0.013}_{-0.01}$	$6.2^{+1.47}_{-0.96}$	$0.89^{+0.48}_{-0.35}$	469 ± 26	17.9	78.7	7.9
MACSJ1311.0-0311	0.494	$0.507^{+0.02}_{-0.015}$	$8.79^{+1.08}_{-0.94}$	$0.39^{+0.15}_{-0.14}$	2083 ± 48	43.6	78.7	7.8
RXJ1524.6+0957	0.516	$0.523^{+0.013}_{-0.014}$	$5.61^{+0.64}_{-0.48}$	$0.34^{+0.14}_{-0.13}$	1974 ± 52	37.7	73.8	8.63
4.6+0957 MS0015.9+1609	0.541	$0.551^{+0.009}_{-0.008}$	$8.37^{+0.32}_{-0.3}$	$0.32^{+0.05}_{-0.05}$	16826 ± 139	121.0	118.1	49.81
MACSJ1423.8+2404	0.543	$0.557^{+0.012}_{-0.012}$	$7.75^{+0.71}_{-0.53}$	$0.31^{+0.1}_{-0.09}$	3518 ± 62	57.2	76.3	14.07
MACSJ1149.5+2223	0.544	$0.544^{+0.012}_{-0.012}$	$12.75^{+1.17}_{-0.96}$	$0.27^{+0.1}_{-0.1}$	9095 ± 109	83.3	150.1	7.13
SC1120-1202	0.562	$0.438^{+0.014}_{-0.016}$	$5.36^{+0.91}_{-0.74}$	$0.57^{+0.32}_{-0.25}$	714 ± 33	21.7	51.7	6.48
MS2053.7-0449	0.583	$0.595^{+0.019}_{-0.019}$	$6.95^{+0.67}_{-0.59}$	$0.2^{+0.11}_{-0.11}$	1884 ± 49	38.5	49.2	3.69
RXJ0956.0+4107	0.587	$0.02^{+0.013}_{-0.012}$	$5.79^{+1.56}_{-1.02}$	$0.79^{+0.81}_{-0.45}$	467 ± 24	19.0	64.0	3.78
MACSJ2129.4-0741	0.589	$0.617^{+0.013}_{-0.015}$	$10.4^{+1.37}_{-1.18}$	$0.57^{+0.16}_{-0.14}$	2918 ± 59	49.1	100.9	18.33
MACSJ0647.7+7015	0.591	$0.052^{+0.013}_{-0.013}$	$7.49^{+0.93}_{-0.61}$	$0.24^{+0.16}_{-0.19}$	2899 ± 58	49.9	78.7	3.52
RXJ0542.8-4100	0.634	$0.657^{+0.035}_{-0.057}$	$8.09^{+1.1}_{-0.95}$	$0.19^{+0.14}_{-0.13}$	1908 ± 50	38.5	64.0	2.04
MACSJ0744.9+3927	0.698	$0.728^{+0.01}_{-0.013}$	$9.61^{+0.77}_{-0.54}$	$0.34^{+0.09}_{-0.08}$	5669 ± 79	71.4	81.2	17.68
RXJ1221.4+4918	0.70	$0.629^{+0.013}_{-0.014}$	$8.16^{+0.84}_{-0.76}$	$0.35^{+0.13}_{-0.11}$	2828 ± 61	46.6	73.8	10.39
RXJ2302.8+0844	0.722	$0.64^{+0.038}_{-0.026}$	$6.6^{+0.92}_{-0.82}$	$0.26^{+0.17}_{-0.15}$	1387 ± 44	31.8	46.7	3.27
RXJ1113.1-2615	0.725	$0.773^{+0.014}_{-0.015}$	$6.1^{+0.83}_{-0.67}$	$0.56^{+0.21}_{-0.18}$	1135 ± 38	29.9	39.4	13.42
MS1137.5+6624	0.782	$0.855^{+0.032}_{-0.03}$	$7.46^{+0.59}_{-0.52}$	$0.34^{+0.12}_{-0.11}$	3957 ± 67	59.1	44.3	10.59
RXJ1350.0+6007	0.804	$0.834^{+0.021}_{-0.019}$	$4.36^{+0.8}_{-0.53}$	$0.65^{+0.36}_{-0.27}$	622 ± 31	20.3	51.7	9.09
RXJ1317.4+2911	0.805	$1.055^{+0.035}_{-0.031}$	$3.84^{+1.24}_{-0.68}$	$0.76^{+0.8}_{-0.5}$	230 ± 20	11.4	29.5	3.05
RXJ1716.4+6708	0.813	$0.834^{+0.013}_{-0.009}$	$6.61^{+0.75}_{-0.66}$	$0.61^{+0.19}_{-0.16}$	1341 ± 40	33.8	44.3	19.28
MS1054.4-0321	0.832	$0.834^{+0.021}_{-0.02}$	$7.27^{+0.48}_{-0.35}$	$0.23^{+0.07}_{-0.07}$	8637 ± 103	83.8	68.9	12.46
WGA1226.9+3332	0.89	$0.197^{+0.027}_{-0.032}$	$7.25^{+0.85}_{-0.69}$	$0.2^{+0.15}_{-0.13}$	2353 ± 51	45.8	66.4	2.55
CLJ1415.1+3612	1.013	$0.965^{+0.034}_{-0.024}$	$6.31^{+0.78}_{-0.6}$	$0.38^{+0.16}_{-0.14}$	1275 ± 39	33.0	36.9	8.53
RXJ0910+5422	1.106	$0.489^{+0.026}_{-0.022}$	$4.1^{+0.92}_{-0.56}$	$0.43^{+0.36}_{-0.25}$	419 ± 24	17.2	24.6	3.69
RXJ1252-2927	1.235	$1.226^{+0.053}_{-0.03}$	$6.9^{+1.2}_{-1.08}$	$0.84^{+0.32}_{-0.28}$	780 ± 33	23.4	32.0	14.56
RXJ0849.9+4452	1.261	$1.304^{+0.054}_{-0.032}$	$4.3^{+1.27}_{-0.71}$	$0.51^{+0.48}_{-0.34}$	327 ± 22	14.6	22.1	2.87
XMM2235.3-2557	1.393	$1.383^{+0.046}_{-0.041}$	$9.6^{+2.0}_{-1.12}$	$0.41^{+0.24}_{-0.21}$	1433 ± 45	31.7	24.6	4.25

Table 2: Best-fit results for our sample of Chandra clusters obtained with a free redshift parameter. The focus is on the best-fit X-ray redshift z_X , compared to the optical value z_o . We also list the X-ray temperature $T(z_X)$ and the abundance $Z_{Fe}(z_X)$. Net photons (0.5-7 keV band) and S/N within the extraction radius R_{ext} are also shown. The value of ΔC_{stat} corresponding to the best-fit z_X value is shown in the last column.